



#### Available online at www.sciencedirect.com

## **ScienceDirect**

Procedia Computer Science 267 (2025) 92-101



www.elsevier.com/locate/procedia

Proceedings of the Third EuroHPC user day

# Large-scale simulations of lattice QCD for nucleon structure using $N_f$ =2+1+1 flavors of twisted mass fermions

C. Alexandrou<sup>a,b</sup>, S. Bacchio<sup>b</sup>, L. Chacon<sup>b</sup>, J. Finkenrath<sup>c</sup>, M. Garofalo<sup>d</sup>, C. Iona<sup>a</sup>, B. Kostrzewa<sup>d</sup>, G. Koutsou<sup>b,\*</sup>, Y. Li<sup>a</sup>, F. Pittler<sup>b</sup>, B. Prasad<sup>b</sup>, A. Sen<sup>d</sup>, C. Urbach<sup>d</sup>

<sup>a</sup>Department of Physics, University of Cyprus, 20536 Nicosia, Cyprus

<sup>b</sup>Computation-based Science and Technology Research Center, The Cyprus Institute, 2121 Nicosia, Cyprus

<sup>c</sup>Theoretical Physics Department, CERN 1211 Geneva 23, Switzerland

<sup>d</sup>Helmholtz-Institut für Strahlen und Kernphysik (Theory), Rheinische Friedrich-Wilhelms-Universität Bonn, Nussallee 14-16, 53115 Bonn,

Germany

### **Abstract**

Understanding the internal structure of protons and neutrons is a fundamental challenge in nuclear physics that requires both theoretical and computational advances. In this work, we present results from large-scale lattice Quantum Chromodynamics (QCD) simulations performed on European supercomputing facilities to calculate key nucleon structure quantities. Our calculations use gauge field configurations with  $N_f$ =2+1+1 twisted mass Wilson-clover fermions at physical quark masses and multiple lattice spacings, allowing for controlled continuum extrapolations. The highly optimized tmLQCD software, combined with the QUDA library for GPU acceleration, enables efficient execution on current heterogeneous computing architectures. We provide details of this computational approach and present our latest results on nucleon structure observables, including nucleon charges, electromagnetic form factors, and momentum fraction. These results include the first continuum extrapolation of nucleon structure quantities using only simulations at physical quark masses, eliminating systematic uncertainties associated with chiral extrapolations.

© 2025 The Authors. Published by Elsevier B.V.
This is an open access article under the CC BY 4.0 license (https://creativecommons.org/licenses/by/4.0)
Peer-review under responsibility of the scientific committee of the Proceedings of the Third EuroHPC user day

Keywords: lattice QCD; nucleon structure; Hybrid Monte Carlo

## 1. Introduction

The strong interactions, described by Quantum Chromodynamics (QCD), bind quarks and gluons to form protons and neutrons, the building blocks of atomic nuclei. Understanding the internal structure of these particles is crucial for advancing nuclear and particle physics, however deriving their properties directly from QCD remains challenging due to its non-perturbative nature at low energies. Lattice QCD provides a first-principles computational framework to tackle this challenge by discretizing space-time on a four-dimensional lattice and numerically evaluating the path

<sup>\*</sup> Corresponding author. Tel.: +357-22-208-633 E-mail address: g.koutsou@cyi.ac.cy

Ensemble	L/a	T/a	~ a [fm]	$\sim M_{\pi} [\text{MeV}]$	β	$c_{\mathrm{sw}}$	К	$a\mu_{\ell}$	$a\mu_{\sigma}$	$a\mu_{\delta}$	$N_{\rm traj}$	τ
cA211.12.48	48	96	0.091	174	1.726	1.7400	0.1400650	0.00120	0.14080	0.15210	2721	1.0
cA211.15.64	64	128	_	194	-	-	0.1400640	0.00150	_	_	3415	-
cA211.15.48	48	96	-	_	_	-	0.1400640	-	_	_	6147	_
cA211.30.32	30	64	-	272	_	-	0.1400645	0.00300	_	_	10234	_
cA211.40.24	24	48	_	315	_	_	0.1400645	0.00400	_	_	4882	_
cA211.53.24	24	48	_	360	_	-	0.1400645	0.00530	_	_	4489	_
cAp211.085.56	56	112	0.087	145	1.745	1.7112	0.1400083	0.00085	0.13839	0.14656	5494	2.0
cAp211.085.48	48	96	_	_	_	_	_	_	_	_	15003	1.0
cB211.072.96	96	192	0.080	140	1.778	1.6900	0.1394267	0.00072	0.1246864	0.1315052	3428	1.0
cB211.072.64	64	128	_	_	_	_	_	_	_	_	3165	_
cB211.072.48	48	96	_	_	_	_	_	_	_	_	3534	_
cB211.14.64	64	128	_	194	_	_	_	0.00140	_	_	4397	1.5
cB211.14.48	48	96	_	_	_	_	_	0.00140	_	_	2897	_
cB211.25.48	48	96	_	260	_	_	_	0.00250	_	_	5349	1.0
cB211.25.32	32	64	_	_	_	_	_	_	_	_	3959	_
cB211.25.24	24	48	_	_	_	_	_	_	_	_	4585	_
cC211.06.112	112	224	0.068	137	1.836	1.6452	0.13875285	0.00060	0.106586	0.107146	1303	1.0
cC211.06.80	80	160	_	_	_	_		_	_	_	3147	_
cC211.20.48	48	96	-	250	-	-		0.00200	_	_	2727	-
cD211.054.128	128	256	0.057	141	1.900	1.6112	0.137972174	0.00054	0.087911	0.086224	838	
cD211.054.96	96	192	_	_	_	-		-	_	_	3386	_
cE211.044.112	112	224	0.049	136	1.960	1.5792	0.137412880	0.00044	0.077707	0.074647	4079	_

Table 1. Algorithmic and bare action parameters of the ETMC  $N_f$ =2+1+1 Wilson clover twisted mass ensembles. Lattice spacing (a) and pion mass  $M_{\pi}$  values are approximate. The trajectory length in molecular dynamics units is given by  $\tau$ . The trajectory counts  $N_{\text{traj}}$  correspond to the state at the time of writing and might have increased since. Dashes (–) indicate that the value from the row above is implied.

integral of QCD through Monte Carlo methods [1]. Lattice QCD calculations involve two computationally intensive stages; first, the generation of gauge field configurations via Markov chain Monte Carlo sampling of the QCD path integral, and second the analysis of these configurations to extract physical observables. Both stages require significant high performance computing resources and specialized algorithms. In this proceeding, we present results from large-scale computational efforts of our Extended Twisted Mass collaboration (ETMC) in both the simulation component and the extraction of nucleon structure quantities using European supercomputing facilities.

For gauge field generation, our simulations use the tmLQCD software package [2, 3, 4] with significant portions of the computation offloaded to GPUs through the QUDA library [5, 6], enabling efficient use of heterogeneous supercomputing resources. For the analysis phase, recent algorithmic advances, including highly optimized multigrid solvers for the inversion of the Dirac operator [7, 8, 9] and effective noise reduction techniques for disconnected quark diagrams [10, 11], have made it possible to perform these calculations directly at physical quark masses, eliminating the need for extrapolations from heavier-than-physical quark masses that introduce uncontrolled systematic errors.

In the remainder of this proceeding, we outline our simulation program and present results for key nucleon structure observables using  $N_f=2+1+1$  twisted mass fermions using exclusively physical quark mass simulations (physical point) with different lattice spacings, providing a first continuum extrapolation of these quantities [12, 13].

## 2. Overview of Current Ensembles

An overview of the current ETMC ensembles, using the  $N_f$ =2+1+1 twisted-mass Wilson clover formulation [14, 15], is listed in Table 1, including the bare parameters of each ensemble. In Figure 1, we plot the available lattice spacings (a) and lattice volumes in terms of  $M_{\pi}L$ , where L is the spatial extent and  $M_{\pi}$  the pion mass. Gradient flow observables are shown in the left panel of Figure 2, whereas the right panel illustrates the evolution of the topological charge, demonstrating that no noticeable freezing is present even at the smallest lattice spacing of  $a \approx 0.049$  fm.

#### 3. Computational Setup

A main component of our computations is the repeated inversion of the twisted-mass Dirac matrix, for which we employ a highly optimized iterative multigrid solver [6, 7], allowing us to efficiently invert the matrix for multiple

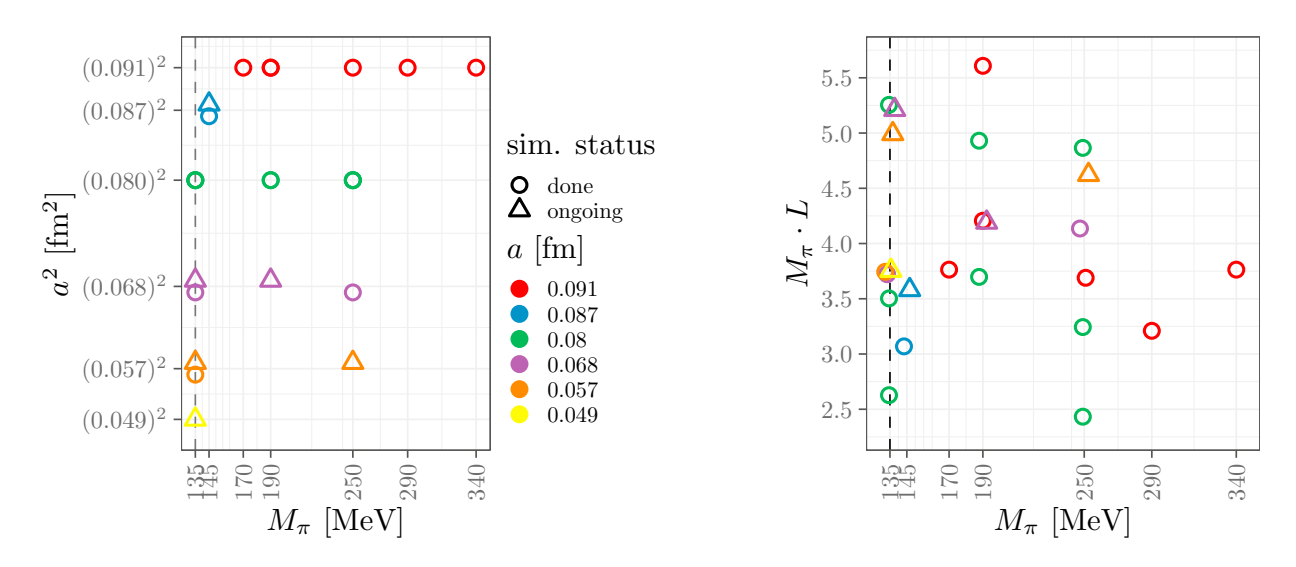


Fig. 1. Overview of all  $N_f$ =2+1+1 ETMC Wilson clover twisted mass ensembles as a function of the pion mass, the lattice spacing and  $M_\pi L$ . Points are slightly displaced either horizontally or vertically to improve visibility. Lattice spacing and pion mass values are approximate.

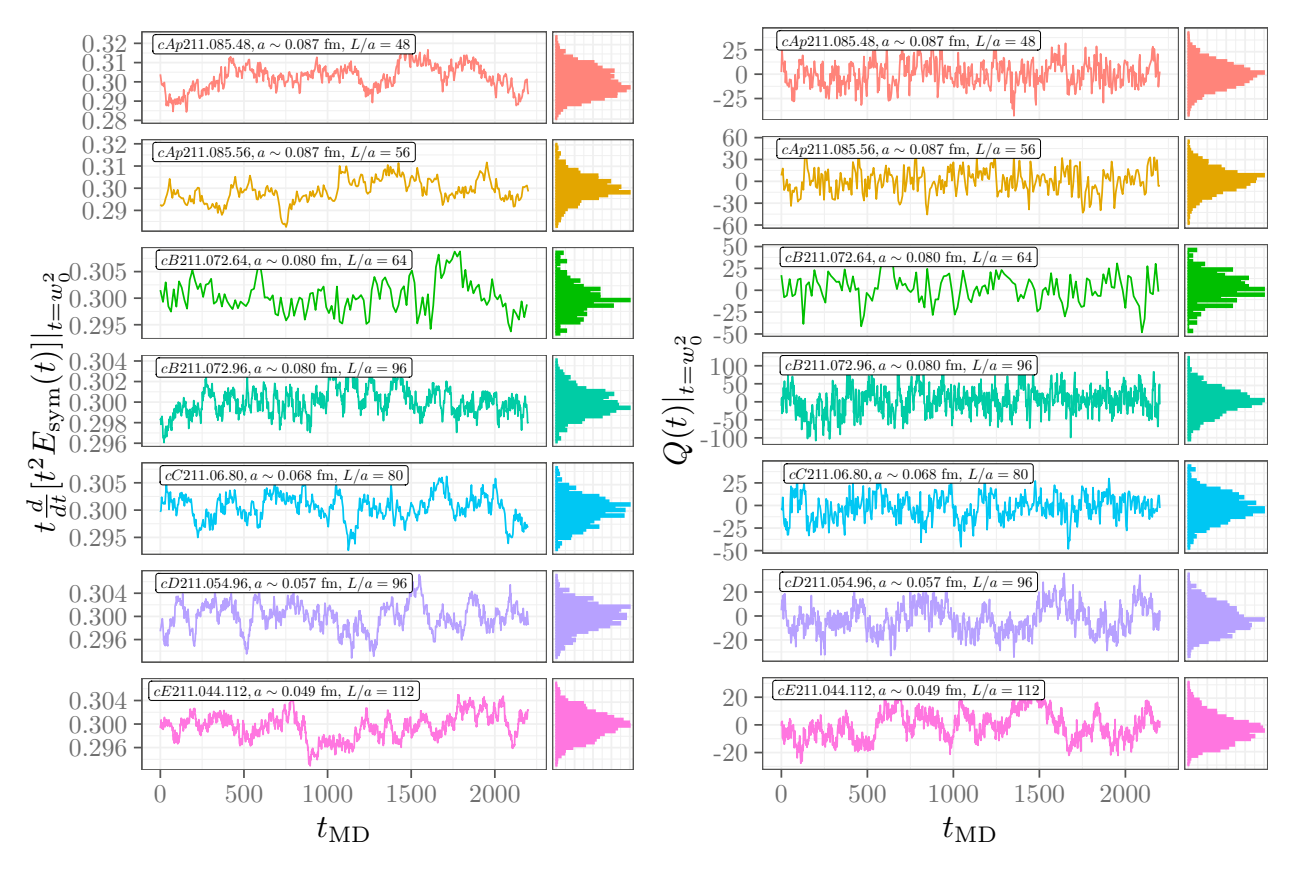


Fig. 2. Left: Molecular dynamics histories for different ensembles close to or at the physical point of the flow-time derivative of the gradient-flowed energy density, interpolated to the flow time where the ensemble average  $t \frac{t}{dt} |t^2 \langle E(t) \rangle| = W(t)|_{t=w_0^2} = 0.3$ . Only the first 2,200 unit-length molecular dynamics units are shown in the histories whereas the histograms in the right sub-panels represent the number of trajectories listed in Table 1. Right: Similar histories for the gradient-flowed topological charge in the clover definition evaluated at a flow time  $t = w_0^2$ .

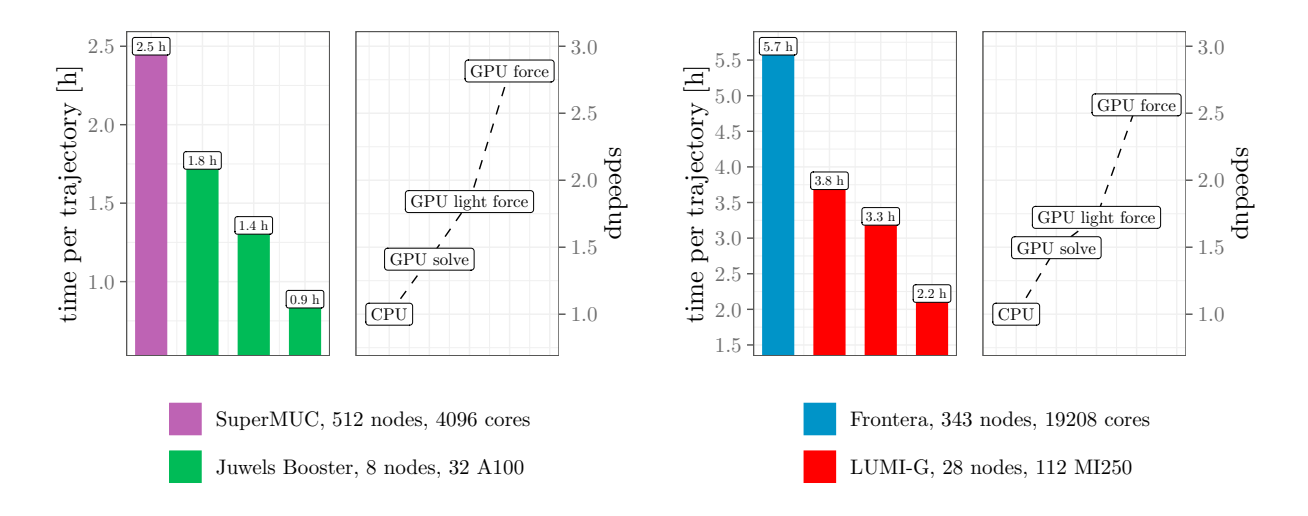


Fig. 3. Left: Time per unit length trajectory of tmLQCD+QUDA (green) for a  $64^3 \times 128$  ensemble at the physical point compared to the CPU machine it was originally generated on (purple) using tmLQCD+DD- $\alpha$ AMG [7]. The different speedups correspond to increasing levels of QUDA offloading. Right: The same comparison, but between tmLQCD+QUDA and tmLQCD+DD- $\alpha$ AMG+QPhiX [16] running a  $112^3 \times 224$  ensemble at the physical point on LUMI-G and Frontera, respectively.

right-hand sides at a reduced cost. Multigrid proceeds by solving the system on coarser grids, using the solution as a preconditioner for the full system and yielding orders of magnitude improvement compared to standard solvers, such as Conjugate Gradient (CG). Within our group, we have developed a multigrid specifically for twisted mass fermions, which allows tuning the twisted mass parameter at each level of the multigrid algorithm [6, 7]. The solver, as implemented in the QUDA community library optimized for multi-GPU systems [5, 17], results in a highly efficient implementation that has allowed us to efficiently carry our these calculations on several flagship European supercomputers. As a first step in interfacing our main code, tmLQCD, to QUDA [4] we offloaded the inversion of the various Dirac operators as well as the gauge force computation. To ensure optimal performance on different GPU architectures we utilize an auto-tuner for the solver parameters [18]. Recently, we further offloaded all computations of the fermionic force. In this way, tmLQCD can reach GPU utilizations over 70% and even up to 90% depending on the number of available CPU cores per GPU. The evolution of the performance of this tmLQCD+QUDA setup is shown in the left panel of Figure 3.

## 4. Nucleon Structure

Understanding nucleon structure is essential for gaining insights into the fundamental properties of QCD. In this section, we briefly introduce our methodology and present representative results of the continuum limit for key nucleon structure observables, using three ensembles at physical values of the pion mass, namely the ensembles cB211.072.64, cC211.060.80, and cD211.054.96 from Table 1. We focus on the isovector axial charge, proton and neutron electromagnetic form factors, and the momentum fraction. i) The nucleon axial charge governs the rate of neutron beta decay and is crucial for tests of the Standard Model's CKM matrix unitarity [12, 19]. Its precise lattice determination serves as a key benchmark due to its well-established experimental value [20]. ii) The electromagnetic form factors of the proton and neutron, which parameterize the distribution of charge and magnetization within these particles, are essential for interpreting electron scattering experiments [21] and resolving puzzles such as the proton radius discrepancy between muonic hydrogen spectroscopy and electron scattering measurements [22, 23]. iii) Quark momentum fractions determine how the nucleon's momentum is distributed among its constituents, providing crucial constraints for parton distribution functions used to interpret high-energy collider experiments [24, 25].

## 4.1. Methodology

Nucleon structure quantities are extracted from matrix elements of local operators between nucleon states. On the lattice, these matrix elements are extracted from correlation functions computed using appropriately defined interpolating operators with the quantum numbers of the nucleon. The standard nucleon interpolating field used in our calculations is  $\mathcal{J}_N(x) = \epsilon^{abc} u^a(x) \left[ u^{bT}(x) C \gamma_5 d^c(x) \right]$ , where u(x) and d(x) are up and down quark fields,  $C = \gamma_0 \gamma_2$  is the charge conjugation matrix, and a, b, c are color indices. For nucleon structure, we compute two- and three-point functions given by

$$C(\Gamma_0, \vec{p}; t_s, t_0) = \sum_{\vec{x}} e^{-i(\vec{x}_s - \vec{x}_0) \cdot \vec{p}} \operatorname{Tr} \left[ \Gamma_0 \langle \mathcal{J}_N(t_s, \vec{x}_s) \bar{\mathcal{J}}_N(t_0, \vec{x}_0) \rangle \right], \text{ and}$$
 (1)

$$C^{\mu}(\Gamma_{\nu}, \vec{q}, \vec{p}'; t_{s}, t_{\text{ins}}, t_{0}) = \sum_{\vec{x}_{\text{ins}}, \vec{x}_{s}} e^{i(\vec{x}_{\text{ins}} - \vec{x}_{0}) \cdot \vec{q}} e^{-i(\vec{x}_{s} - \vec{x}_{0}) \cdot \vec{p}'} \text{Tr} \left[ \Gamma_{\nu} \langle \mathcal{J}_{N}(t_{s}, \vec{x}_{s}) O^{\mu}(t_{\text{ins}}, \vec{x}_{\text{ins}}) \bar{\mathcal{J}}_{N}(t_{0}, \vec{x}_{0}) \rangle \right], \tag{2}$$

where  $t_0$  is the source time,  $t_s$  is the sink time,  $\Gamma_0 = \frac{1}{2}(1 + \gamma_0)$  is the unpolarized projector and  $\Gamma_k = i\Gamma_0\gamma_5\gamma_k$  with k = 1, 2, 3 are polarized projectors,  $O^{\mu}$  is the operator of interest inserted at time  $t_{\text{ins}}$ ,  $\vec{q}$  is the momentum transfer,  $\vec{p}'$  is the sink momentum, and the traces are over spinor indices.

Three-point functions receive contributions from both so-called connected and disconnected diagrams. The former correspond to the operator being inserted on one of the valence quarks, while the latter involve operator insertions on sea quarks, resulting in quark loops. The evaluation of disconnected diagrams is computationally very demanding, requiring advanced noise reduction techniques [26]. For the connected contributions, we use standard techniques involving the computation of the sequential propagator through the sink. In this approach, the sink-source time separation, the projector and the momentum at the sink  $\vec{p}$ , are kept fixed. For the disconnected contributions, we employ stochastic techniques combined with dilution schemes, hierarchical probing [11], and deflation of low modes [27]. To illustrate the scale of computations required, Table 2 shows the statistics used for calculating the connected three-point functions for our three ensembles. As the sink-source separation  $t_s$  increases, we increase the number of source positions to maintain similar statistical precision. Indicatively, for the statistics given in Table 2 we find a relative statistical error between 0.8% to 2% depending on the value of the time ( $t_s$ ) for the nucleon isovector axial three-point function. The computational resources required are approximately 250,000 GPU-hours for B64, 550,000 GPU-hours for C80, and 600,000 GPU-hours for D96, in units of NVIDIA A100 GPU-hours. This means that the analysis of the connected contributions alone for a single ensemble, requires resources comparable to an annual extreme scale allocation for this statistical accuracy.

Ens. ID (short name)	Vol.	<i>a</i> [fm]	$N_{\rm conf}$	$(t_s/a)_{N_{\rm src}}$	$N_{\rm src}^{\rm 2p}$
cB211.072.64 (B64)	64×128	0.080	750	$8_1, 10_2, 12_5, 14_{10}, 16_{32}, 18_{112}, 20_{128}$	477
cC211.060.80(C80)	$80 \times 160$	0.068	400	$6_1$ , $8_2$ , $10_4$ , $12_{10}$ , $14_{22}$ , $16_{48}$ , $18_{45}$ , $20_{116}$ , $22_{246}$	650
cD211.054.96 (D96)	96×192	0.057	500	$8_1, 10_2, 12_4, 14_8, 16_{16}, 18_{32}, 20_{64}, 22_{16}, 24_{32}, 26_{64}$	480

Table 2. We show details of the ensembles analyzed, including their short name (first column), lattice volume (second column), lattice spacing in fm (third column), number of configurations analyzed (fourth column), sink-source separations ( $t_s/a$ ) analyzed for the connected three-point functions with number of source positions per configuration ( $N_{src}$ ) indicated as a subscript (fifth column), and number of source positions per configuration analyzed for the two-point function ( $N_{src}$ ).

For the disconnected contributions, we use the techniques and parameters shown in Table 3. The calculation of quark loops is particularly intensive, requiring specialized algorithms and significant computational resources.

As in the case of the simulations, the most demanding component of our nucleon structure program is the inversion of the twisted-mass Dirac matrix to obtain the quark propagators which are in turn contracted appropriately to produce

	cB211.072.64					cC21	1.060.	80	cD211.054.96			
Flavor	$N_{ m defl}$	$N_r$	$N_{ m Had}$	$N_{ m vect}$	$N_{ m defl}$	$N_r$	$N_{\mathrm{Had}}$	$N_{ m vect}$	$N_{\rm defl}$	$N_r$	$N_{\mathrm{Had}}$	$N_{\mathrm{vect}}$
Light	200	1	512	6144	450	1	512	6144	0	8	512	49152
Strange	0	2	512	12288	0	4	512	24576	0	4	512	24576
Charm	0	12	32	4608	0	1	512	6144	0	1	512	6144

Table 3. Parameters and statistics used for the evaluation of the disconnected three-point functions, for the same  $N_{\rm conf}$  as Table 2. For each ensemble, in the columns from left to right we give: i) the number of deflated eigenvectors  $N_{\rm def}$ , ii) the number of stochastic sources  $N_r$ , iii) the number of Hadamard vectors  $N_{\rm Had}$ , and iv) the total number of computed vectors,  $N_{\rm vect}$ , which after color and spin dilution are obtained via  $12 \times N_r \times N_{\rm Had}$ .

the nucleon two- and three-point functions. For each configuration and source position listed in Tables 2 and 3, we require O(10) inversions of the Dirac matrix, meaning for any given ensemble we require  $O(10^6)$  inversions. The multigrid solver via QUDA is crucial in this step, as it allows us to efficiently solve for the required number right hand sides within a typical annual allocation on a range of supercomputing systems, as shown in the left panel of Figure 4.

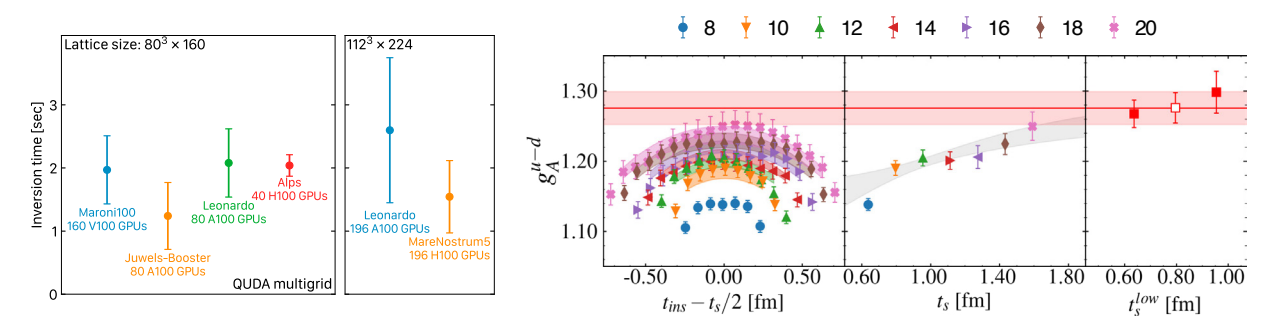


Fig. 4. Left: Time per inversion of the QUDA multigrid solver when using the C80 and E112 ensembles on European supercomputers. The bars indicate the standard deviation over a number of inversions spanning between hundreds of thousands to millions, depending on the system. Right: Excited state analysis for determining the isovector axial charge  $g_A^{u-d}$  on the cB211.072.64 ensemble. Left panel: Ratio data for different source-sink separations  $t_s$  (different symbols) as a function of the insertion time shifted by  $t_s/2$ . The bands show two-state fits. Middle panel: Ratio values for  $t_{\text{ins}} = t_s/2$ , with the grey band showing the predicted time-dependence from the two-state fit. Right panel: Extracted values of  $g_A^{u-d}$  using different two-state fit ranges. The open symbol indicates the selected value, with the red band showing its statistical error.

The two- and three-point functions contain contributions from the ground state as well as excited states. Their spectral decomposition takes the form,  $C(\vec{p},t_s) = \sum_i c_i(\vec{p})e^{-E_i(\vec{p})t_s} + \cdots$  and  $C^{\mu}(\Gamma_{\nu},\vec{p}',\vec{p},t_s,t_{\rm ins}) = \sum_{i,j} \mathcal{R}^{i,j}_{\mu}(\Gamma_{\nu},\vec{p}',\vec{p}) \times e^{-E_i(\vec{p}')(t_s-t_{\rm ins})-E_j(\vec{p})t_{\rm ins}} + \cdots$ , respectively, where  $E_i(\vec{p})$  is the energy of the *i*-th state with momentum  $\vec{p}$ , and  $\mathcal{R}^{i,j}_{\mu}$  are the transition matrix elements. To isolate the ground state contribution, we form the ratio:

$$R^{\mu}(\Gamma_{\nu}, \vec{p}', \vec{p}; t_{s}, t_{\text{ins}}) = \frac{C^{\mu}(\Gamma_{\nu}, \vec{p}', \vec{p}; t_{s}, t_{\text{ins}})}{C(\Gamma_{0}, \vec{p}'; t_{s})} \sqrt{\frac{C(\Gamma_{0}, \vec{p}; t_{s} - t_{\text{ins}})C(\Gamma_{0}, \vec{p}'; t_{\text{ins}})C(\Gamma_{0}, \vec{p}'; t_{s})}{C(\Gamma_{0}, \vec{p}'; t_{s} - t_{\text{ins}})C(\Gamma_{0}, \vec{p}; t_{\text{ins}})C(\Gamma_{0}, \vec{p}; t_{s})}}.$$
(3)

In the limit of large Euclidean time separations, this ratio yields the desired ground state matrix element,  $\Pi^{\mu}(\Gamma_{\nu}; \vec{p}', \vec{p})$ , i.e.  $R^{\mu}(\Gamma_{\nu}, \vec{p}', \vec{p}; t_{s}, t_{ins}) \xrightarrow{t_{s} - t_{ins} \gg a} \Pi^{\mu}(\Gamma_{\nu}; \vec{p}', \vec{p})$ . In practice, we cannot take the time separations arbitrarily large due to the exponential increase of the relative statistical errors. Therefore, to ensure ground state dominance, we explicitly include contributions from excited states, fitting the two- and three-point functions to forms including terms for both ground and excited states [12]. In many cases, we find the excited state energies extracted from fits to two-point functions cannot fully describe the excited-states in three-point functions, as also predicted from chiral perturbation theory [28]. Therefore, we allow different excited state energies in the two- and three-point functions, which is critical for reliably extracting ground state matrix elements. The right panel of Figure 4 shows an example of our excited state analysis for the isovector axial charge  $g_{A}^{\mu-d}$  on the cB211.072.64 ensemble. The right panel, which shows

the extracted  $g_A^{u-d}$  values from the two-state fit as we increase the smallest sink-source separation, demonstrates the convergence of our analysis. For our final result, we use a model averaging procedure based on the Akaike Information Criterion (AIC) [29] to combine results from different fit ranges and ansätze, which allows us to reliably estimate both statistical and systematic uncertainties.

#### 4.2. Isovector nucleon matrix elements in the continuum limit

As mentioned, in the results that follow we take the continuum limit using three ensembles with different lattice spacings and approximately the same physical volume of about (5 fm)<sup>3</sup> [30, 12]. The nucleon axial charge  $g_A^{u-d}$ 

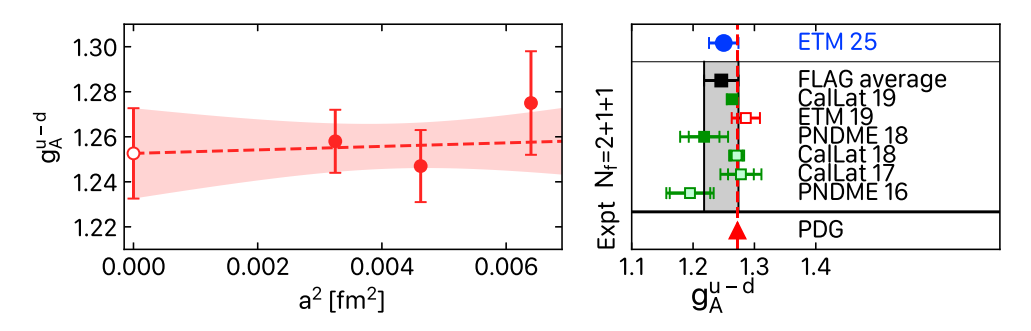


Fig. 5. Left: Continuum extrapolation of the isovector axial charge  $g_A^{u-d}$ . The filled symbols represent results from individual ensembles, while the open symbol shows the extrapolated value at the continuum limit. Right: Comparison of our result for  $g_A^{u-d}$  with other lattice QCD results and with their average as done in the recent FLAG review [31].

is defined as the nucleon matrix element of the isovector axial current at zero momentum transfer,  $\langle N|\bar{u}\gamma_{\mu}\gamma_{5}u-\bar{d}\gamma_{\mu}\gamma_{5}d|N\rangle=g_{A}^{u-1}\bar{u}_{N}\gamma_{\mu}\gamma_{5}u_{N}$ , where  $u_{N}$  is a nucleon spinor. This quantity determines the rate of neutron beta decay and is measured to high precision experimentally, making it an important benchmark for lattice QCD calculations. In the left panel of Figure 5 we show our continuum extrapolation of the isovector axial charge. Our final result in the continuum limit is  $g_{A}^{u-d}=1.250(24)$  [13], which is in excellent agreement with the experimental value of  $g_{A}^{u-d}=1.2754(13)$  [20]. We also compare our result to lattice QCD results as aggregated by the Flavor Lattice Averaging Group (FLAG) in their most recent review [31], published prior to our result.

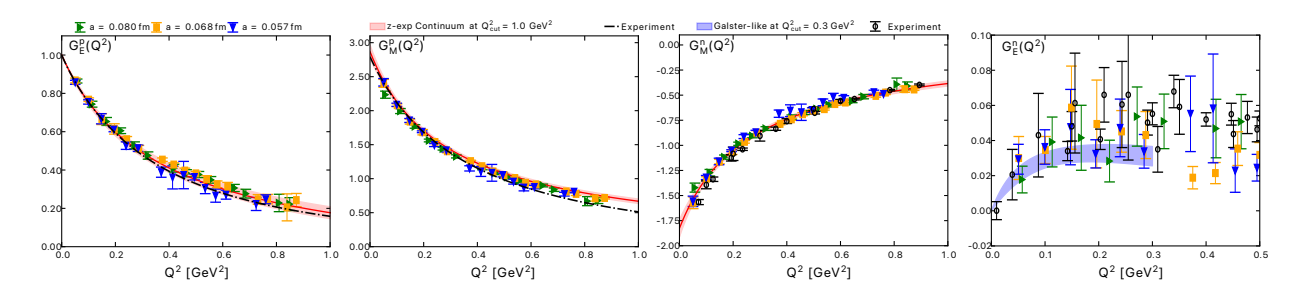


Fig. 6. From left to right, the proton electric, magnetic, and neutron magnetic and electric form factors as functions of  $Q^2$ , for the three ensembles (green, yellow, and blue points with decreasing a) and at the continuum limit (red and blue bands). Black dashed lines for the proton and black circles for the neutron show a collection of recent experimental results.

The electromagnetic form factors parameterize the nucleon matrix element of the electromagnetic current, yielding the Dirac and Pauli form factors,  $F_1(Q^2)$  and  $F_2(Q^2)$ , respectively, where  $Q^2$  is the momentum transfer squared. These can be rewritten in terms of the electric and magnetic Sachs form factors,  $G_E(Q^2) = F_1(Q^2) + \frac{Q^2}{4m_N^2}F_2(Q^2)$  and  $G_M(Q^2) = F_1(Q^2) + F_2(Q^2)$ . We calculate both isovector and isoscalar form factors, accounting for disconnected contributions in the latter, and combine them to obtain proton and neutron form factors [21, 32]. Figure 6 shows the  $Q^2$  dependence of the proton and neutron electromagnetic form factors and their continuum limit. We extract the electric and magnetic radii of the proton (p) and neutron (n), i.e.  $\langle r_E^2 \rangle^{p/n}$  and  $\langle r_M^2 \rangle^{p/n}$ , as well as the magnetic moments  $(\mu_p)$  and

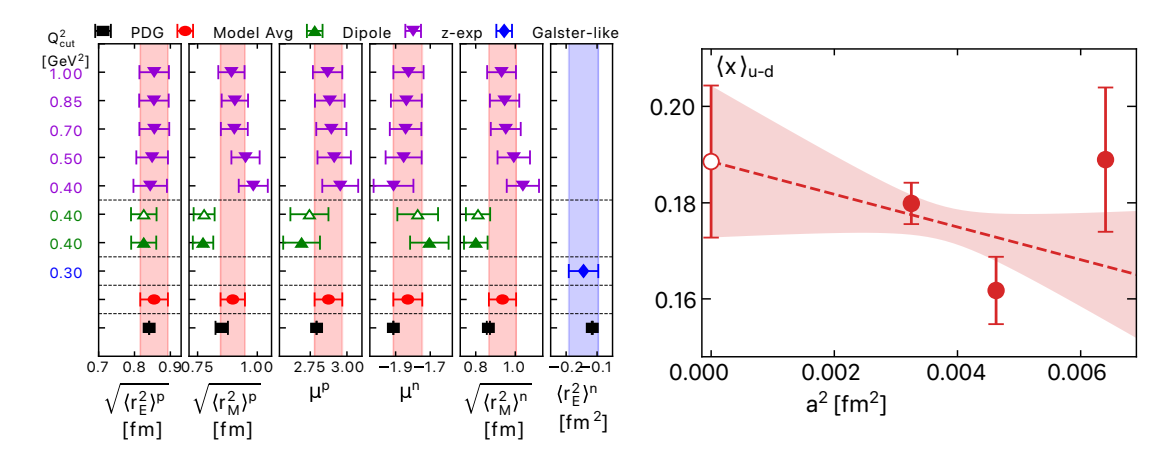


Fig. 7. Left: Electric and magnetic radii and magnetic moments of the proton and neutron for all  $Q_{\text{cut}}^2$  for the z-expansion (purple downward-pointing triangles) and, in the dipole case, using both one-step (filled green triangle) or two-step (open green triangle) approaches. The blue diamond and blue band corresponds to Galster-like fit to  $G_E^n$ . The red point and band denoted "Model average" is obtained by weighting according to the AIC. Right: Continuum extrapolation of the isovector momentum fraction  $\langle x \rangle_{u-d}$ . The filled symbols represent results from individual ensembles, while the open symbol shows the extrapolated value at the continuum limit.

 $\mu_n$ ), using a range of  $Q^2 \to 0$  extrapolations, including varying the maximum  $Q^2$  value used, varying the fit function between the so-called z-expansion and dipole forms, and via either a one-step extrapolation, where the dependence in  $Q^2$  and  $Q^2$  are fitted simultaneously, or a two-step extrapolation, where the  $Q^2$ -dependence is fitted first for the three ensembles and then the continuum extrapolation is taken in a second step. More details are provided in Ref. [32]. The results are shown in the left panel of Figure 7 and are compared to the experimentally determined values.

The average momentum fraction carried by quarks in the nucleon,  $\langle x \rangle^q$ , is obtained from the forward matrix element of the traceless part of the energy-momentum tensor,  $\langle N(p)|\bar{q}\gamma_{(\mu}iD_{\nu)}q|N(p)\rangle = \langle x \rangle^q \bar{u}_N(p)\gamma_{(\mu}p_{\nu)}u_N(p)$ , where  $\{\cdots\}$  denotes symmetrization and subtraction of the trace [33, 30]. Figure 7 shows our continuum extrapolation of the isovector combination of the momentum fraction,  $\langle x \rangle^{u-d}$ . Our final result in the continuum limit is  $\langle x \rangle^{u-d} = 0.171(18)$  [30], which is in good agreement with recent phenomenological determinations from NNPDF [34], JAM [35], and CTEQ-TEA using data from LHC [36].

## 5. Conclusions

We have presented an overview of our large-scale lattice QCD calculations for both simulations and analysis using European supercomputing facilities. Our gauge field generation program has successfully produced multiple ensembles with  $N_f$ =2+1+1 twisted mass Wilson-clover fermions at physical quark masses and with varying lattice spacings, enabled by the highly optimized tmLQCD software package with GPU acceleration through QUDA. Significant computational improvements have resulted in GPU utilization of up to 90%, depending on the target machine.

The analysis of these gauge configurations has yielded precise determinations of key nucleon structure observables, including the axial charge, electromagnetic form factors, and momentum fraction. These results, enabled by large scale computational resources such as those provided by EuroHPC, are the first to include continuum limit extrapolations exclusively using simulations with physical quark masses. This represents a significant advancement, since so far such results included simulations with heavier-than-physical quark masses, thus requiring a modeling of the quark mass dependence of the nucleon structure quantities, which in turn introduced an unknown systematic error.

Current computational efforts are focused on incorporating results with finer lattice spacing, namely the cE211.044.112 ensemble in our analysis, with  $a\approx0.049$  fm, which will further improve the robustness of our continuum extrapolations and reduce overall systematic uncertainties. As an indicative example, preliminary results for the isovector tensor charge,  $\langle N|\bar{u}\sigma_{\mu\nu}u-\bar{d}\sigma_{\mu\nu}\gamma_5d|N\rangle=g_T^{u-d}\bar{u}_N\sigma_{\mu\nu}u_N$ , available at low statistics are shown in Figure 8. This continued progress in both simulation methodology and analysis techniques promises to deliver increasingly pre-

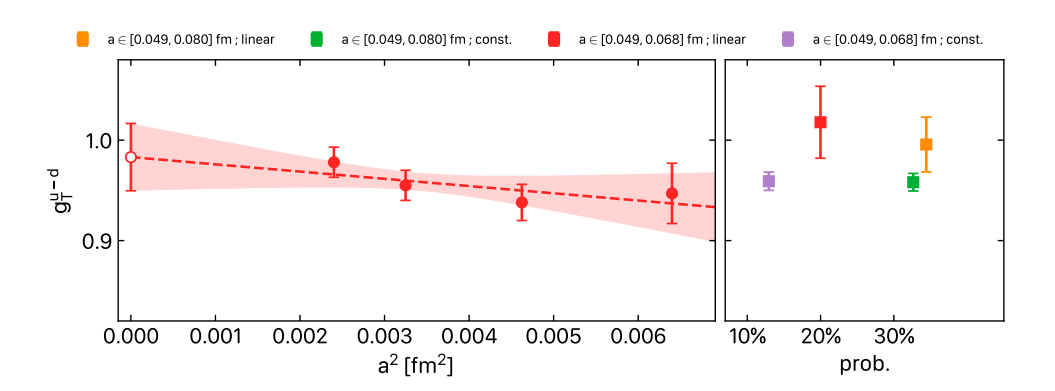


Fig. 8. Continuum limit of the isovector tensor charge  $g_T^{u-d}$  with preliminary results for the cE211.044.112 ensemble included. We vary between linear and constant fits as described in the figure title, and show the value obtained from each fit and its probability in the right panel.

cise determinations of hadron properties directly from QCD, contributing to our fundamental understanding of strong interaction physics.

## Acknowledgements

We acknowledge EuroHPC Joint Undertaking for awarding the projects with ID EHPC-EXT-2023E02-052 with access to MareNostrum5, EHPC-REG-2022R02-094 and EHPC-REG-2023R03-187 with access to Meluxina, EHPC-EXT-2022E01-033 access to Leonardo and EHPC-REG-2021R0095 access to LUMI. The authors also gratefully acknowledge access to the Marvin cluster of the University of Bonn and support by the HRZ-HPC team and acknowledge the Texas Advanced Computing Center (TACC) at the University of Texas at Austin for proving HPC resources on Frontera (Project ID PHY21001). C.A. and G.K. acknowledge partial support from the European Joint Doctorate AQTIVATE (Grant Agreement No. 101072344). C. A., S. B., G. K., and F. P. acknowledge support by the projects "IMAGE-N" (EXCELLENCE/0524/0459), "Baryon8" (POSTDOC/0524/0001), "HyperON" (VISION ERC-PATH 2/0524/0001), "MuonHVP" (EXCELLENCE/0524/0459), "PulseQCD" (EXCELLENCE/0524/0269), and "DeNuTra" (EXCELLENCE/0524/0455), co-financed by the European Regional Development Fund and the Republic of Cyprus through the Research and Innovation Foundation. L. C. and B. P. are supported by ENGAGE, which received funding from the EU's Horizon 2020 Research and Innovation Programme under the Marie Skłodowska-Curie GA No.101034267. J. F. acknowledges financial support from the Next Generation Triggers project. B. K. and A. S. acknowledge financial support by CRC 1639 NuMeriQS - project no. 511713970.

#### References

- [1] J. Finkenrath, Review on Algorithms for dynamical fermions, PoS LATTICE2022 (2023) 227. arXiv:2402.11704, doi:10.22323/1.430.0227.
- [2] K. Jansen, C. Urbach, tmLQCD: A Program suite to simulate Wilson Twisted mass Lattice QCD, Comput. Phys. Commun. 180 (2009) 2717–2738. arXiv:0905.3331, doi:10.1016/j.cpc.2009.05.016.
- [3] A. Abdel-Rehim, F. Burger, A. Deuzeman, K. Jansen, B. Kostrzewa, L. Scorzato, C. Urbach, Recent developments in the tmLQCD software suite, PoS LATTICE2013 (2014) 414. arXiv:1311.5495, doi:10.22323/1.187.0414.
- [4] B. Kostrzewa, S. Bacchio, J. Finkenrath, M. Garofalo, F. Pittler, S. Romiti, C. Urbach, Twisted mass ensemble generation on GPU machines, PoS LATTICE2022 (2023) 340. arXiv:2212.06635, doi:10.22323/1.430.0340.
- [5] M. A. Clark, R. Babich, K. Barros, R. C. Brower, C. Rebbi, Solving Lattice QCD systems of equations using mixed precision solvers on GPUs, Comput. Phys. Commun. 181 (2010) 1517–1528. arXiv:0911.3191, doi:10.1016/j.cpc.2010.05.002.
- [6] M. A. Clark, B. Joó, A. Strelchenko, M. Cheng, A. Gambhir, R. Brower, Accelerating Lattice QCD Multigrid on GPUs Using Fine-Grained Parallelization (12 2016). arXiv:1612.07873.
- [7] C. Alexandrou, S. Bacchio, J. Finkenrath, A. Frommer, K. Kahl, M. Rottmann, Adaptive Aggregation-based Domain Decomposition Multigrid for Twisted Mass Fermions, Phys. Rev. D 94 (11) (2016) 114509. arXiv:1610.02370, doi:10.1103/PhysRevD.94.114509.
- [8] S. Bacchio, C. Alexandrou, J. Finkerath, Multigrid accelerated simulations for Twisted Mass fermions, EPJ Web Conf. 175 (2018) 02002.arXiv:1710.06198, doi:10.1051/epjconf/201817502002.

- [9] C. Alexandrou, S. Bacchio, J. Finkenrath, Multigrid approach in shifted linear systems for the non-degenerated twisted mass operator, Comput. Phys. Commun. 236 (2019) 51–64. arXiv:1805.09584, doi:10.1016/j.cpc.2018.10.013.
- [10] C. McNeile, C. Michael, Decay width of light quark hybrid meson from the lattice, Phys. Rev. D 73 (2006) 074506. arXiv:hep-lat/0603007, doi:10.1103/PhysRevD.73.074506.
- [11] A. Stathopoulos, J. Laeuchli, K. Orginos, Hierarchical probing for estimating the trace of the matrix inverse on toroidal lattices (2013). arXiv:1302.4018.
- [12] C. Alexandrou, S. Bacchio, M. Constantinou, J. Finkenrath, R. Frezzotti, B. Kostrzewa, G. Koutsou, G. Spanoudes, C. Urbach, Nucleon axial and pseudoscalar form factors using twisted-mass fermion ensembles at the physical point, Phys. Rev. D 109 (3) (2024) 034503. arXiv: 2309.05774, doi:10.1103/PhysRevD.109.034503.
- [13] C. Alexandrou, S. Bacchio, J. Finkenrath, C. Iona, G. Koutsou, Y. Li, G. Spanoudes, Nucleon charges and  $\sigma$ -terms in lattice QCD, Phys. Rev. D 111 (5) (2025) 054505. arXiv:2412.01535, doi:10.1103/PhysRevD.111.054505.
- [14] C. Alexandrou, et al., Simulating twisted mass fermions at physical light, strange and charm quark masses, Phys. Rev. D 98 (5) (2018) 054518. arXiv:1807.00495, doi:10.1103/PhysRevD.98.054518.
- [15] J. Finkenrath, et al., Twisted mass gauge ensembles at physical values of the light, strange and charm quark masses, PoS LATTICE2021 (2022) 284. arXiv: 2201.02551, doi:10.22323/1.396.0284.
- [16] M. Schröck, S. Simula, A. Strelchenko, Accelerating Twisted Mass LQCD with QPhiX, PoS LATTICE2015 (2016) 030. arXiv:1510.08879, doi:10.22323/1.251.0030.
- [17] R. Babich, M. A. Clark, B. Joo, G. Shi, R. C. Brower, S. Gottlieb, Scaling lattice QCD beyond 100 GPUs, in: International Conference for High Performance Computing, Networking, Storage and Analysis, 2011. arXiv:1109.2935, doi:10.1145/2063384.2063478.
- [18] M. Garofalo, B. Kostrzewa, S. Romiti, A. Sen, Autotuning multigrid parameters in the HMC on different architectures, PoS LATTICE2024 (2025) 276. doi:10.22323/1.466.0276.
- [19] C. Alexandrou, M. Constantinou, K. Hadjiyiannakou, K. Jansen, C. Kallidonis, G. Koutsou, A. Vaquero Aviles-Casco, Nucleon axial form factors using  $N_f = 2$  twisted mass fermions with a physical value of the pion mass, Phys. Rev. D96 (5) (2017) 054507. arXiv:1705.03399, doi:10.1103/PhysRevD.96.054507.
- [20] S. Navas, et al., Review of particle physics, Phys. Rev. D 110 (3) (2024) 030001. doi:10.1103/PhysRevD.110.030001.
- [21] C. Alexandrou, S. Bacchio, M. Constantinou, J. Finkenrath, K. Hadjiyiannakou, K. Jansen, G. Koutsou, A. V. A. Casco, Proton and neutron electromagnetic form factors from lattice QCD (2018). arXiv:1812.10311.
- [22] R. Pohl, et al., The size of the proton, Nature 466 (2010) 213–216. doi:10.1038/nature09250.
- [23] V. Punjabi, C. F. Perdrisat, M. K. Jones, E. J. Brash, C. E. Carlson, The Structure of the Nucleon: Elastic Electromagnetic Form Factors, Eur. Phys. J. A 51 (2015) 79. arXiv:1503.01452, doi:10.1140/epja/i2015-15079-x.
- [24] C. Alexandrou, M. Constantinou, K. Hadjiyiannakou, K. Jansen, F. Manigrasso, Flavor decomposition for the proton helicity parton distribution functions, Phys. Rev. Lett. 126 (10) (2021) 102003. arXiv:2009.13061, doi:10.1103/PhysRevLett.126.102003.
- [25] C. Alexandrou, et al., Moments of nucleon generalized parton distributions from lattice QCD simulations at physical pion mass, Phys. Rev. D 101 (3) (2020) 034519. arXiv:1908.10706, doi:10.1103/PhysRevD.101.034519.
- [26] C. Alexandrou, M. Constantinou, V. Drach, K. Hadjiyiannakou, K. Jansen, G. Koutsou, A. Strelchenko, A. Vaquero, Evaluation of disconnected quark loops for hadron structure using GPUs, Comput. Phys. Commun. 185 (2014) 1370–1382. arXiv:1309.2256, doi:10.1016/j.cpc.2014.01.009.
- [27] A. S. Gambhir, A. Stathopoulos, K. Orginos, Deflation as a Method of Variance Reduction for Estimating the Trace of a Matrix Inverse, SIAM J. Sci. Comput. 39 (2017) A532–A558. arXiv:1603.05988, doi:10.1137/16M1066361.
- [28] O. Bär, Nπ-state contamination in lattice calculations of the nucleon axial form factors, Phys. Rev. D 99 (5) (2019) 054506. arXiv:1812. 09191, doi:10.1103/PhysRevD.99.054506.
- [29] W. I. Jay, E. T. Neil, Bayesian model averaging for analysis of lattice field theory results, Phys. Rev. D 103 (2021) 114502. arXiv:2008.01069, doi:10.1103/PhysRevD.103.114502.
- [30] C. Alexandrou, S. Bacchio, M. Constantinou, J. Finkenrath, K. Hadjiyiannakou, K. Jansen, G. Koutsou, A. Vaquero Aviles-Casco, Nucleon axial, tensor, and scalar charges and σ-terms in lattice QCD, Phys. Rev. D 102 (5) (2020) 054517. arXiv:1909.00485, doi:10.1103/PhysRevD.102.054517.
- [31] Y. Aoki, et al., FLAG Review 2024 (11 2024). arXiv: 2411.04268.
- [32] C. Alexandrou, S. Bacchio, G. Koutsou, B. Prasad, G. Spanoudes, Proton and neutron electromagnetic form factors using Nf=2+1+1 twisted-mass fermions with physical values of the quark masses, PoS LATTICE2024 (2025) 332. arXiv:2502.11301, doi:10.22323/1.466.0332.
- [33] C. Alexandrou, M. Constantinou, K. Hadjiyiannakou, K. Jansen, C. Kallidonis, G. Koutsou, A. Vaquero Avilés-Casco, C. Wiese, Nucleon Spin and Momentum Decomposition Using Lattice QCD Simulations, Phys. Rev. Lett. 119 (14) (2017) 142002. arXiv:1706.02973, doi: 10.1103/PhysRevLett.119.142002.
- [34] R. D. Ball, et al., Parton distributions from high-precision collider data, Eur. Phys. J. C 77 (10) (2017) 663. arXiv:1706.00428, doi: 10.1140/epjc/s10052-017-5199-5.
- [35] N. Sato, C. Andres, J. J. Ethier, W. Melnitchouk, Strange quark suppression from a simultaneous Monte Carlo analysis of parton distributions and fragmentation functions, Phys. Rev. D 101 (7) (2020) 074020. arXiv:1905.03788, doi:10.1103/PhysRevD.101.074020.
- [36] T.-J. Hou, et al., New CTEQ global analysis of quantum chromodynamics with high-precision data from the LHC, Phys. Rev. D 103 (1) (2021) 014013. arXiv:1912.10053, doi:10.1103/PhysRevD.103.014013.